

A Study of Microphysical Mechanisms for Correlation Patterns between Droplet Radius and Optical Thickness of Warm Clouds with a Spectral Bin Microphysics Cloud Model

KENTAROH SUZUKI

Department of Atmospheric Science, Colorado State University, Fort Collins, Colorado

TERUYUKI NAKAJIMA

Center for Climate System Research, University of Tokyo, Chiba, Japan

TAKASHI Y. NAKAJIMA

Research and Information Center, Tokai University, Tokyo, Japan

ALEXANDER P. KHAIN

Institute of Earth Sciences, Hebrew University of Jerusalem, Jerusalem, Israel

(Manuscript received 6 August 2009, in final form 13 October 2009)

ABSTRACT

This study investigates the correlation patterns between cloud droplet effective radius (CDR) and cloud optical thickness (COT) of warm clouds with a nonhydrostatic spectral bin microphysics cloud model. Numerical experiments are performed with the model to simulate low-level warm clouds. The results show a positive and negative correlation pattern between CDR and COT for nondrizzling and drizzling stages of cloud development, respectively, consistent with findings of previous observational studies. Only a positive correlation is simulated when the collection process is switched off in the experiment, whereas both the positive and negative correlations are reproduced in the simulation with collection as well as condensation processes. The positive and negative correlations can also be explained in terms of an evolution pattern of the size distribution function due to condensation and collection processes, respectively.

Sensitivity experiments are also performed to examine how the CDR–COT correlation patterns are influenced by dynamical and aerosol conditions. The dynamical effect tends to change the amplitude of the CDR–COT plot mainly through changing the liquid water path, whereas the aerosol amount significantly modifies the correlation pattern between CDR and COT mainly through changing the cloud particle number concentration. These results suggest that the satellite-observed relationships between CDR and COT can be interpreted as being formed through microphysical particle growth processes under various dynamical and aerosol conditions in the real atmosphere.

1. Introduction

The climatic effects of warm clouds are characterized by their optical and microphysical properties, which are represented by parameters such as cloud droplet effective radius (CDR) and cloud optical thickness (COT). These two cloud parameters have been observed by

remote sensing technique from aircraft (e.g., Nakajima et al. 1991; Asano et al. 1995; Brenguier et al. 2000) and satellite (e.g., Han et al. 1994; Nakajima and Nakajima 1995; Kawamoto et al. 2001), and there have been found characteristic relationships between CDR and COT of warm clouds.

Nakajima et al. (1991) found that the CDR and COT tend to be positively correlated when the cloud does not include drizzle-sized particles, whereas they tend to be negatively correlated when a significant concentration of drizzle particle exists in the cloud. The positive correlation for nondrizzling clouds indicates that the cloud

Corresponding author address: Kentaroh Suzuki, Department of Atmospheric Science, Colorado State University, Fort Collins, CO 80523-1371.
E-mail: kenta@atmos.colostate.edu

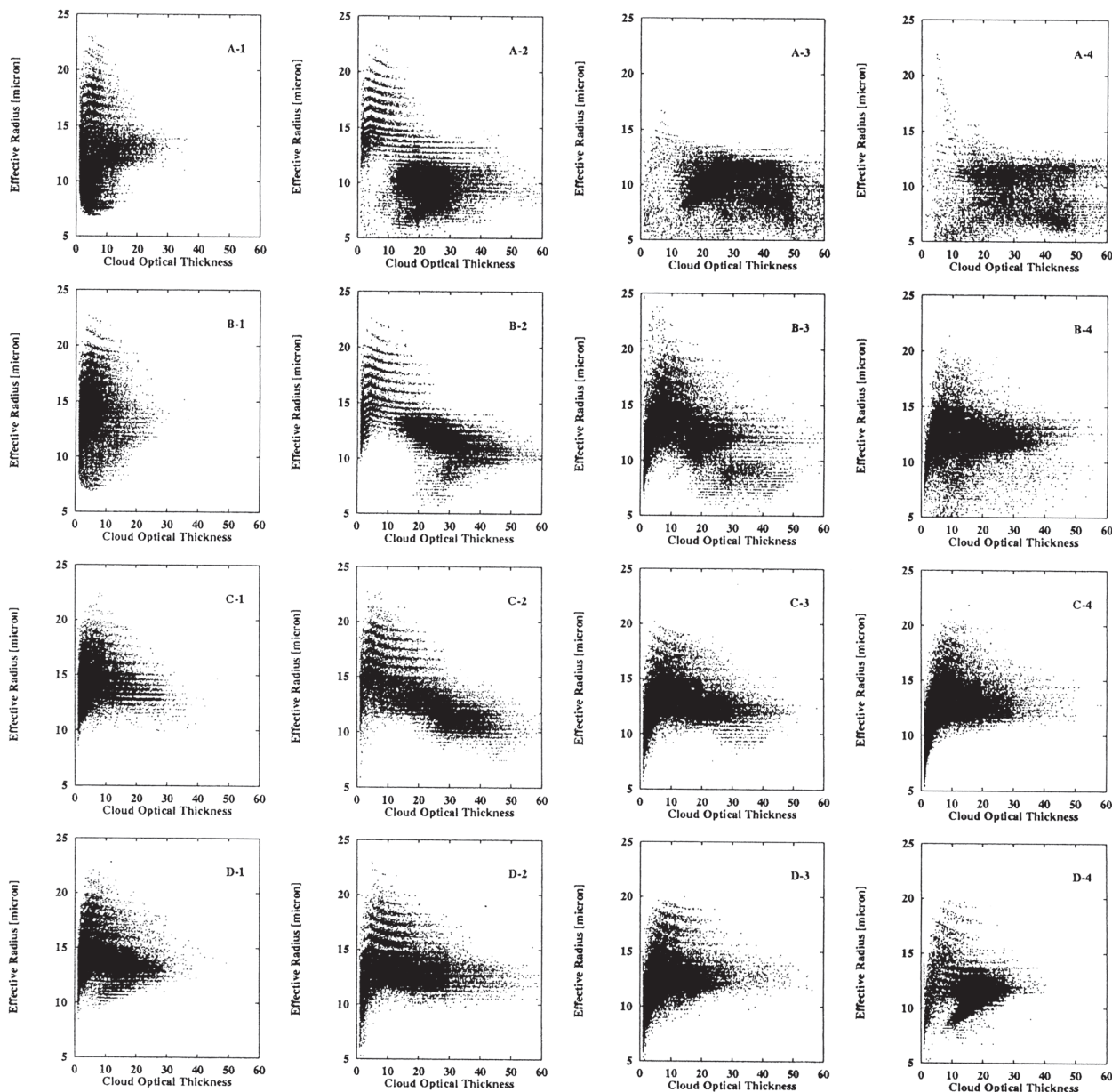


FIG. 1. Scatterplots of cloud droplet effective radius (CDR) versus cloud optical thickness (COT) obtained from satellite remote sensing over the FIRE region (cited from Nakajima and Nakajima 1995).

becomes optically thicker with growth of cloud particle, whereas the negative correlation for drizzling clouds indicates that the cloud becomes optically thinner with particle growth, possibly due to the conversion process of cloud water into drizzle or rainwater. These correlation patterns can be interpreted to reflect cloud microphysical processes that take place within the clouds.

These statistical analyses have been extended into wider regions by Nakajima and Nakajima (1995), who reported that the First International Satellite Cloud Climatology Project (ISCCP) Regional Experiment (FIRE)

region is dominated by negative correlations, in contrast to the Atlantic Stratocumulus Transition Experiment (ASTEX) region, where positive correlation tendencies are mainly found. These correlation statistics are shown here in Fig. 1 for the FIRE region and Fig. 2 for the ASTEX region, both cited from Nakajima and Nakajima (1995). Figures 1 and 2 show various different relationships between CDR and COT, implying more complicated microphysical mechanisms involved in the clouds over these regions. Several other observational studies have demonstrated complex positive and negative correlation

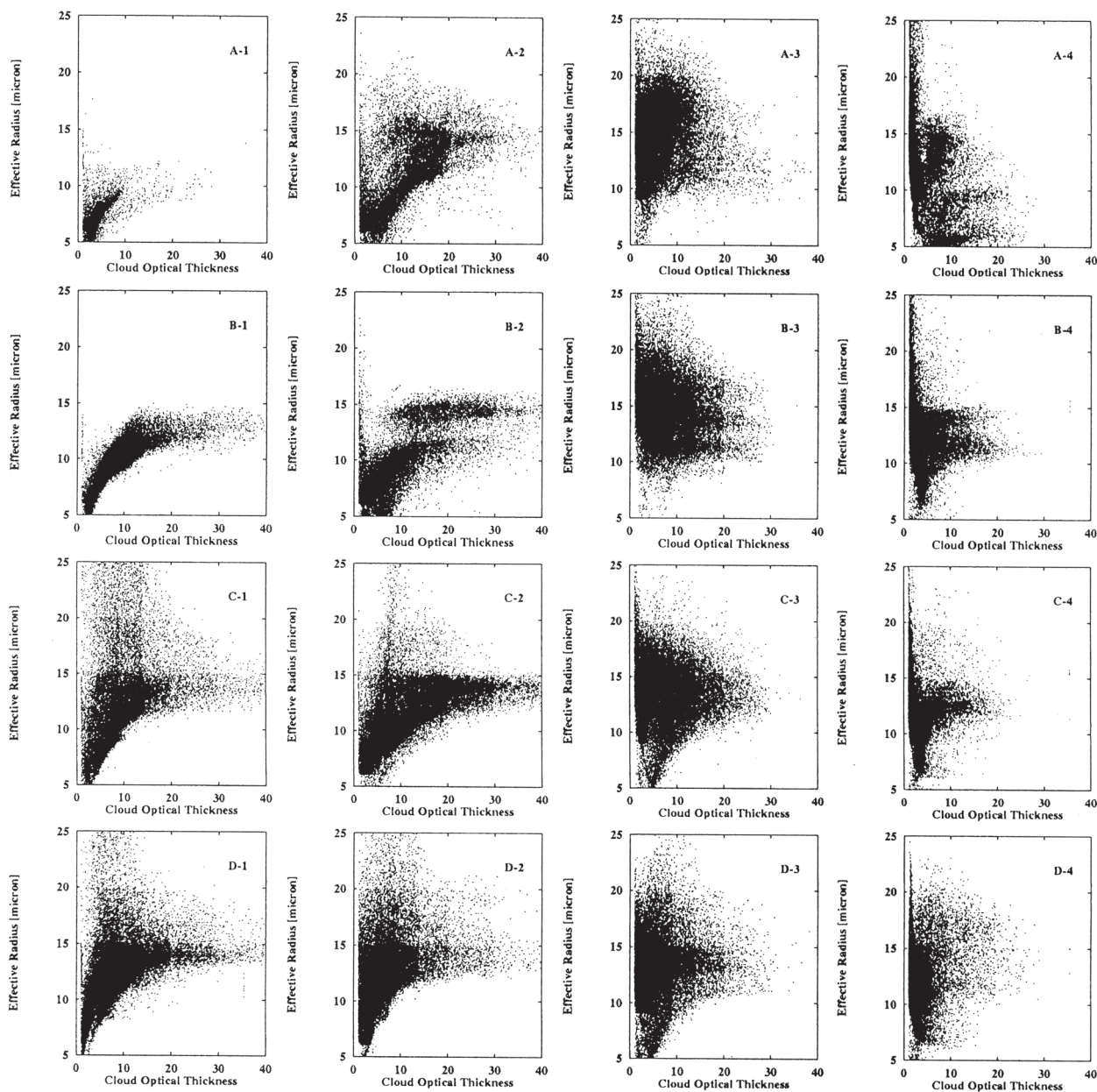


FIG. 2. As in Fig. 1, but for the ASTEX region (cited from Nakajima and Nakajima 1995).

patterns between CDR and COT (Han et al. 1994, 1998; Asano et al. 1995; Boers and Rotstajn 2001; Kawamoto et al. 2001; Szczodrak et al. 2001; Peng et al. 2002; Lebsock et al. 2008; Kobayashi and Masuda 2008).

Since the shortwave radiative property strongly depends on CDR and COT (e.g., Slingo 1989), clouds with positive and negative CDR–COT correlations should have largely different radiative properties. It is therefore important to understand how these correlation patterns are formed and what mechanisms are responsible for determining the CDR–COT relationships. Recent

observational studies also showed that the microphysical characteristics of warm clouds significantly change from region to region associated with differing conditions of aerosol amount and static stability (e.g., Masunaga et al. 2002; Matsui et al. 2004). In this regard, it is also important to investigate how the CDR–COT relationships are influenced by these environmental factors.

For these purposes, it is useful to employ numerical cloud models. Lohmann et al. (2000) performed a numerical simulation with a general circulation model (GCM) and

reported that the simulated CDR and COT are positively and negatively correlated for nonprecipitating and precipitating clouds, respectively. Their finding is consistent with previous observational studies mentioned above and implies that their GCM includes some mechanisms that may reproduce the observed CDR–COT relationships. In GCMs, however, the cloud microphysics is crudely represented by simple bulk parameterizations with coarse resolutions of several hundreds of kilometers, which are not sufficient for fully understanding the microphysical mechanisms responsible for the CDR–COT statistics.

Motivated by this difficulty with GCMs, our previous study (Suzuki et al. 2006) employed a cloud model with a more detailed representation of microphysical processes, based on a bin-type microphysics scheme that predicts the size distribution function of cloud particles in an explicit manner, and highlighted the statistics of CDR and COT obtained from the simulation with the model. The results showed that the positive and negative correlation patterns are simulated for nondrizzling and drizzling clouds, respectively, similar to the previous observational studies mentioned above, and reproduced the CDR–COT scatterplots that closely resemble the observed statistics over FIRE and ASTEX regions when pristine and polluted air conditions, respectively, are assumed.

The present study intends to provide more detailed descriptions of our previous study (Suzuki et al. 2006) using the bin-type cloud model. The main focus of this study is on fundamental mechanisms as to how these positive and negative correlation patterns are formed through microphysical processes of warm clouds. In this paper, we demonstrate that the condensation and collection particle growth processes are responsible for the positive and negative correlation patterns, respectively. We also show how the aerosol amount and dynamical conditions influence the correlation patterns based on sensitivity experiments of changing these environmental conditions, thereby providing a basis for interpreting the satellite-observed correlation statistics as shown in Figs. 1 and 2. The findings of this study may also be helpful to improve the bulk parameterizations employed in GCMs.

This paper first describes the nonhydrostatic spectral microphysics cloud model employed in the present study in section 2. The cloud model is then used for numerical simulation of warm clouds with the experimental design shown in section 3. The simulated results are analyzed with a focus on the correlation patterns between CDR and COT and their formation mechanisms in section 4. The results of the sensitivity experiments of changing the dynamical and aerosol conditions are presented in

section 5. These simulation results are then used to interpret the correlation statistics observed by Nakajima and Nakajima (1995) in section 6. Section 7 summarizes the conclusions of this study.

2. The cloud model

The model used in this study is a nonhydrostatic spectral bin microphysics cloud model developed by Suzuki (2004) and Suzuki et al. (2006) and originally based on the Hebrew University Cloud Model (e.g., Khain and Sednev 1996; Khain et al. 1999; Khain and Pokrovsky 2004; Khain et al. 2004). This is a coupled model of the nonhydrostatic dynamical framework and the spectral bin cloud microphysics module. This model is similar to the cloud models that have recently been developed and used for various numerical simulations with detailed representations of microphysical processes (e.g., Feingold et al. 1999; Feingold and Kreidenweis 2002; Takahashi and Kawano 1998; Takahashi and Shimura 2004; Iguchi et al. 2008). The present model has also been used in a recent study of Sato et al. (2009) that implemented a Monte Carlo integration method into collection processes. The basic features of this model are described in this section.

The nonhydrostatic dynamical equations are numerically solved to predict the atmospheric density ρ , horizontal wind u , vertical wind w , and internal energy e by using the scheme developed by Stone and Norman (1992) with the addition of gravity force. This is based on an operator splitting method with an explicit time integration scheme. The Cartesian coordinate is used in the present model with a staggered grid system in which the wind components and scalar variables are located at the edge and the center of the grid point, respectively. The advection processes for density, momentum, energy, and water vapor are calculated by the Van Leer (1977) scheme.

The cloud microphysics processes involving the size distribution functions are calculated with a bin-type scheme based on Khain and Sednev (1996) and Khain et al. (1999, 2004), taking into account the microphysical processes of warm clouds (i.e., nucleation from aerosol, condensational growth, and collection processes). In the bin-type microphysics scheme, the size distribution functions of cloud particles are predicted in an explicit manner as explained below.

The nucleation process is calculated from the size distribution function of hygroscopic aerosols, which is also predicted in the model. The part of aerosol spectra greater than the critical size is activated to grow into cloud particles. This critical radius of aerosol is calculated from the supersaturation S according to the

TABLE 1. Notations of symbols used in this paper.

Variable	Meaning
ρ	Atmospheric density
u	Horizontal wind velocity
w	Vertical wind velocity
p	Pressure
e	Internal energy per volume
T	Temperature
m	Particle mass
r	Liquid particle radius
$f(m, t)$	Size distribution function of liquid particle
$f_{\text{CCN}}(m, t)$	Size distribution function of aerosols serving as CCN
$r_{N,\text{crit}}$	Critical radius of aerosol for activation
S	Super saturation with regard to liquid
σ	Surface tension of water
R_v	Gas constant of water vapor
i	Van 't Hoff coefficient
ρ_s	Density of aerosol matter
ρ_w	Density of liquid water
m_s	Molecular weight of aerosol matter
m_w	Molecular weight of water
L	Latent heat for vaporization
K	Coefficient of thermal conductivity of air
D	Diffusion coefficient of water vapor
$e^*(T)$	Saturation vapor pressure
q	Cloud water content
r_e	Cloud effective particle radius
τ_c	Cloud optical thickness
W	Liquid water path
N_c	Cloud droplet number concentration
λ	Adiabatic parameter

Köhler theory as follows (see Table 1 for explanations of symbols):

$$r_{N,\text{crit}} = \left(\frac{4 A^3 1}{27 B S^2} \right)^{1/3}, \quad A = \frac{2\sigma}{R_v \rho_w T}, \quad \text{and}$$

$$B = i \frac{\rho_s m_w}{\rho_w m_s}.$$

The sulfate aerosol (ammonium sulfate) is assumed for chemical species in the simulation. The number of aerosol particles belonging to the size bin beyond the critical size is moved to the size bin of liquid particle r_{liquid} that corresponds to the aerosol particle size r_{CCN} according to the relationship obtained from the Köhler curve analysis as

$$r_{\text{liquid}} = \sqrt{\frac{3Br_{\text{CCN}}^3}{A}}.$$

The cloud particles thus formed by the nucleation process continue to grow through the condensation process. The change in size distribution function by condensation process is given as (e.g., Rogers and Yau 1989)

$$\left[\frac{\partial f}{\partial t} \right]_{\text{cond/evap}} = \frac{\partial}{\partial t} f(m, t) = -\frac{\partial}{\partial m} \left[f(m, t) \frac{dm}{dt} \right], \quad (1)$$

where the growth speed is determined from the supersaturation S as

$$\frac{dm}{dt} = rG(p, T)S, \quad G(p, T) = \frac{4\pi}{\left(\frac{L}{R_v T} - 1 \right) \frac{L}{KT} + \frac{R_v T}{De^*(T)}}. \quad (2)$$

In the present model, we adopt the numerical scheme of Bott (1989) for solving (1) because of its numerical stability and positive definiteness.

The cloud particles grow also because of the collection process, for which the tendency of size distribution function is given as (e.g., Rogers and Yau 1989)

$$\left[\frac{\partial f}{\partial t} \right]_{\text{collcoag}} = \frac{\partial}{\partial t} f(m, t)$$

$$= \frac{1}{2} \int_0^m K(m - m', m') f(m - m', t) f(m', t) dm'$$

$$- f(m, t) \int_0^\infty K(m, m') f(m', t) dm'. \quad (3)$$

The numerical scheme of Bott (1998) is adopted for the solution of (3) since the scheme is positive definite and conservative. The collection kernel function $K(m_1, m_2)$ describes the efficiency of collection between the particles with sizes m_1 and m_2 and characterizes the evolution pattern of size distribution function by collection process. There are several forms of the kernel function suggested by previous studies. In the present study, we perform experiments by assuming the form suggested by Long (1974) as

$$K(m_1, m_2) = \begin{cases} C_1 (v_{\text{large}}^2 + v_{\text{small}}^2) & \text{for } r_{\text{large}} < 50 \mu\text{m}, \\ C_2 (v_{\text{large}} + v_{\text{small}}) & \text{for } r_{\text{large}} \geq 50 \mu\text{m}, \end{cases} \quad (4)$$

where r_{large} denotes the radius of larger particle, and v_{large} and v_{small} are the volumes of larger and smaller particles, respectively. The constants C_1 and C_2 are set as $9.44 \times 10^9 \text{ cm}^{-3} \text{ s}^{-1}$ and $5.78 \times 10^3 \text{ s}^{-1}$, respectively, following Long (1974). Equation (4) means that the collection process has a threshold behavior. The collection process is not active when the both particles are smaller than the critical size ($50 \mu\text{m}$) and discontinuously becomes active for the particles exceeding the critical size.

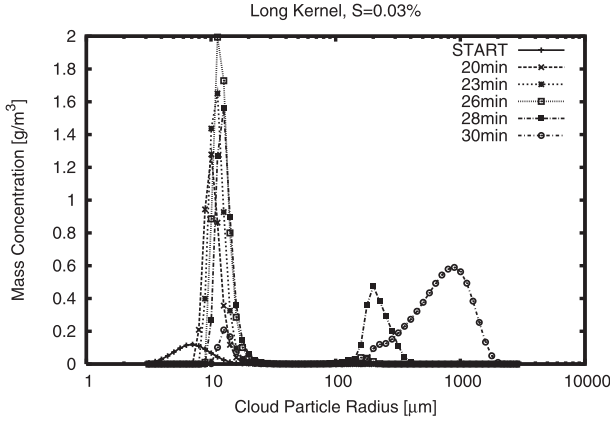


FIG. 3. Time evolution of size distribution function driven by the condensation and collection processes predicted by the present model for a given supersaturation value of $S = 0.03\%$.

An example of the evolution of size distribution function due to condensation and collection processes is shown in Fig. 3 when this form of collection kernel function is used. It is illustrated that the size spectrum becomes narrow in the early stage of evolution as induced by condensation process and then produces a bimodal feature, including a drizzle mode as well as a cloud mode. This is due to the drastic increase in collection efficiency with particle size when it becomes greater than the critical radius. This bimodal behavior with the remarkable drizzle mode is likely to represent the characteristics of observed size spectra, which often tend to be bimodal. As will be demonstrated later (in section 4), the distinctive difference in evolution pattern of the size spectra between early and mature growth stages is closely related to different correlation patterns between CDR and COT.

3. Warm cloud simulation

The numerical experiment is performed using the cloud model described in the previous section to form a low-level warm cloud, which is qualitatively similar to those studied by Nakajima and Nakajima (1995). We conducted a two-dimensional experiment by giving a horizontally homogeneous initial condition as described below. For simulating a warm cloud confined to lower layer, a stable condition in the upper layer and an unstable layer in the lower atmosphere are initially assumed as

$$T(z) = \begin{cases} -\Gamma_1 z + T_{\text{sfc}} & \text{for } z < z_c, \\ -\Gamma_2(z - z_c) + T(z_c) & \text{for } z \geq z_c, \end{cases} \quad (5)$$

where T_{sfc} and z_c denote the surface temperature and the critical height of the lower unstable layer, respectively.

The lapse rate Γ_2 is assumed to be 2 K km^{-1} , and Γ_1 is changed from 7.5 to 8.5 K km^{-1} in sensitivity experiments to examine the dynamical effects. The temperature profile given by (5) is shown in Fig. 4a for the case of $T_{\text{sfc}} = 300 \text{ K}$, $z_c = 1 \text{ km}$, $\Gamma_1 = 7.5 \text{ K km}^{-1}$ and $\Gamma_2 = 2 \text{ K km}^{-1}$. The vertical shear of horizontal wind is also given in the initial condition as shown in Fig. 4b. The initial humidity profile is given with the scale height of 1 km as shown in Fig. 4c.

We initially assume a Junge-type size distribution function for aerosol particle as

$$f_{\text{CCN}}(z, r) = f_0(z) \left(\frac{r}{r_0} \right)^{-3},$$

where $r_0 = 0.1 \mu\text{m}$ and $f_0(z)$ is given by an exponential decay profile as

$$f_0(z) = f_{\text{sfc}} \exp\left(-\frac{z}{H}\right),$$

where f_{sfc} and H denote the surface value of f_0 and the scale height, respectively. We assume various values of f_{sfc} ranging from $f_{\text{sfc}} = 10^5$ to 10^7 m^{-3} for investigating the aerosol effect on the cloud property, and the scale height H is set as 1 km . The values of $f_{\text{sfc}} = 10^5$ and 10^7 m^{-3} approximately correspond to the surface aerosol number concentration of $n_a = 10^8 \text{ m}^{-3}$ and 10^{10} m^{-3} , respectively, and also to column aerosol particle numbers of $N_a = 10^{11}$ and 10^{13} m^{-2} , respectively, with a 1-km scale height. A warm bubble is initially located to trigger the convection and the cloud formation as a potential temperature perturbation given by

$$\Delta\theta = \Delta\theta_0 \cos^2 \left[\frac{\pi}{2} \sqrt{\left(\frac{x - x_0}{x_r} \right)^2 + \left(\frac{z - z_0}{z_r} \right)^2} \right],$$

where $x_0 = 9 \text{ km}$, $z_0 = 0.5 \text{ km}$, $x_r = 5 \text{ km}$, $z_r = 0.5 \text{ km}$, and $\Delta\theta = 1 \text{ K}$. The computational domain is set as 30 km in the horizontal and 5 km in the vertical direction, and the resolutions are 500 m in the horizontal and 50 m in the vertical. The time integration is performed with the time step of 1 s for 2 h to cover the period of formation of a single warm cloud. Although these experimental designs are simpler than those giving a forcing from a boundary layer field experiment (e.g., Bretherton et al. 1999), it is more convenient to simulate a single warm cloud in a manner as simple as possible for our purpose of obtaining the fundamental understandings of complicated microphysical processes within the cloud. More realistic experimental settings, however, are necessary in future studies for investigating

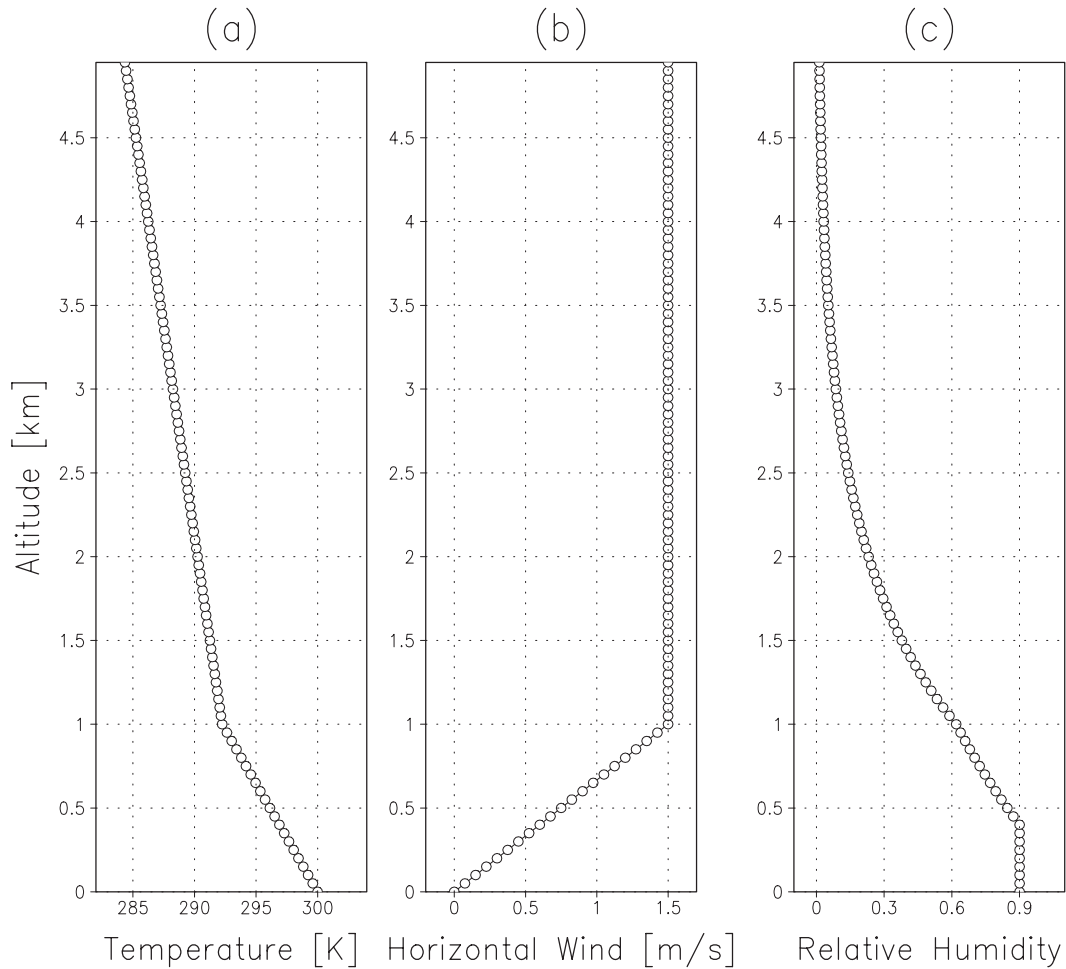


FIG. 4. Initial profiles of (a) temperature, (b) horizontal wind, and (c) relative humidity assumed for the simulations.

how the findings of this study based on relatively simple simulations would be applied to more realistic and complicated situations.

We prepare 20 bins ranging from 0.01 to 1 μm for aerosol particles and 60 bins ranging from 3 to 3000 μm for liquid cloud particles. We divide the cloud size distribution into three parts (i.e., 3–50, 50–500, and 500–3000 μm) and represent each range as the cloud, drizzle, and rainwater part, respectively. The mass concentration of cloud, drizzle, and rain are explicitly calculated by integrating the simulated size distribution function over these ranges.

The cloud optical thickness τ_c and effective particle radius r_e can also be explicitly calculated from the simulated size distribution function $f(x, z, r)$ for each grid point (x, z) by their definitions as

$$\tau_c(x) = \int_{z=z_B}^{z=z_T} \int_{r=3\mu\text{m}}^{r=50\mu\text{m}} Q_{\text{ext}} f(x, z, r) \pi r^2 dr dz,$$

$$r_e(x, z) = \frac{\int_{r=3\mu\text{m}}^{r=50\mu\text{m}} f(x, z, r) r^3 dr}{\int_{r=3\mu\text{m}}^{r=50\mu\text{m}} f(x, z, r) r^2 dr},$$

where Q_{ext} is the extinction coefficient factor and is equal to 2 in a good approximation for cloud particles, and z_B and z_T denote the cloud base and top, respectively. Because the value of r_e obtained from remote sensing represents the cloud particle size at an optical depth of 20%–40% of the total optical thickness (Nakajima and King 1990), we adopt a simulated value of r_e at the upper 30% of τ_c so that the calculated values can be compared with the remote sensing results.

4. Correlation statistics between CDR and COT

a. Positive and negative correlation patterns

Figure 5 shows the scatterplot between CDR and COT obtained from the simulation, separately for nondrizzling

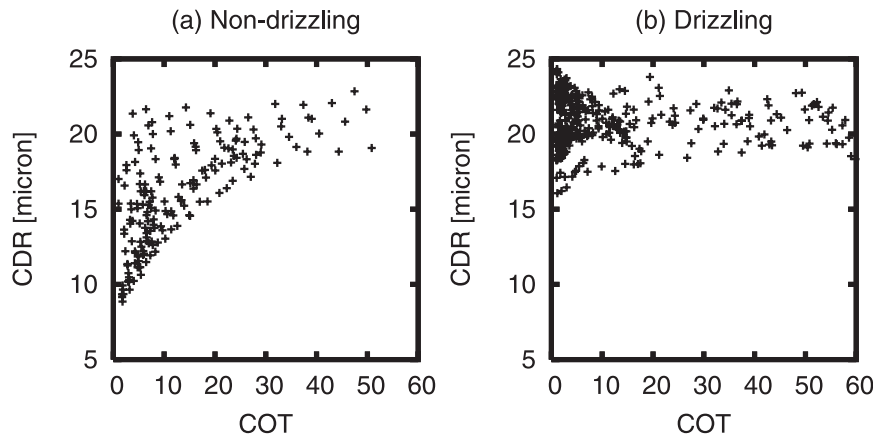


FIG. 5. Scatterplot of CDR versus COT obtained from the simulation for (a) nondrizzling and (b) drizzling stages.

(Fig. 5a) and drizzling (Fig. 5b) stages that are defined as the cloud states including the drizzle water content smaller and larger than 10^{-3} g m^{-3} , respectively. This result is obtained from the simulations with $\Gamma_1 = 8.0 \text{ K km}^{-1}$ and f_{sic} ranging from $7.8 \times 10^5 \text{ m}^{-3}$ to $1.8 \times 10^6 \text{ m}^{-3}$, approximately corresponding to the column aerosol particle number $N_a \sim 10^{12} \text{ m}^{-2}$. Each point in the plot represents a cloud profile at a particular horizontal point and a particular time.

It is found in the figure that the COT tends to increase with increasing CDR in nondrizzling stages (Fig. 5a), leading to a positive correlation between them, whereas the COT tends to moderately decrease with increasing CDR in drizzling stages (Fig. 5b), depicting a negative correlation. These characteristics are closely similar to the observed CDR–COT statistics reported by Nakajima et al. (1991; see their Fig. 10) and those shown in Figs. 1 and 2 reported by Nakajima and Nakajima (1995), suggesting that the present model can reproduce the observed correlation patterns. This result also confirms that the positive and negative correlations relate to the presence of drizzle-sized particles as found by Nakajima et al. (1991).

b. Microphysical interpretation

To investigate how the CDR and COT tend to change at different stages of cloud development, we show in Fig. 6 the tendencies of these quantities, which are defined as their time derivatives, as vectors projected on the CDR–COT plane. The figure shows the results from the simulations with collection as well as condensation processes (Fig. 6a) and with condensation process only (Fig. 6b), where the collection process is switched off in the model. It is shown in Fig. 6a that both COT and CDR have positive tendencies over the area of $\text{COT} < 20$ and $\text{CDR} < 20 \mu\text{m}$, whereas the negative tendencies of COT

concurrent with positive tendencies of CDR are found over the area of $5 < \text{COT} < 20$ and $\text{CDR} > 20 \mu\text{m}$. These characteristics confirm the notion that the CDR and COT are positively and negatively correlated for early nondrizzling stage and mature drizzling stage of cloud development, respectively. Another interesting feature found in Fig. 6a is negative tendencies of both CDR and COT over the area of $\text{COT} < 5$ and $\text{CDR} > 15 \mu\text{m}$. These tendencies are found over later times corresponding to the decaying stage after the precipitation occurs, when the evaporation process typically take place in the model.

In the case of condensation only (Fig. 6b), the vector arrows become close to horizontal over the area of $\text{CDR} > 20 \mu\text{m}$ and thus the negative correlation part tends to vanish. The increasing and decreasing tendencies of both CDR and COT can also be found in this case since the condensation and evaporation processes take place for early and decaying stages, respectively, without the collection stage. It is worth noting that the CDR values are limited to smaller than about $21 \mu\text{m}$ in this case, demonstrating that the particle growth is significantly suppressed compared to the cases with collection processes (Fig. 6a). These results suggest that the negative correlation pattern is formed through the collection process whereas the positive correlation pattern is formed by the condensation process.

These tendencies of CDR and COT found at specific stages of cloud development can be schematically summarized (see Fig. 7). The COT tends to increase with increasing CDR at early stage of cloud development, providing a positive correlation pattern between them as shown by the arrow A. At the drizzling growth stage shown by the arrow B, the COT tends to decrease with increasing CDR and these two quantities are negatively correlated. This branch B is typically followed by the

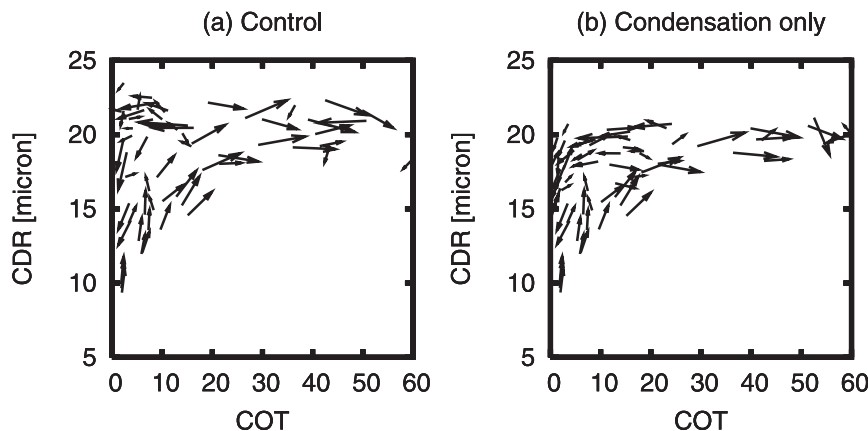


FIG. 6. Vector charts describing the tendencies of CDR and COT obtained from the simulations (a) with both condensation and collection growth processes and (b) with condensation process only.

arrow C, which represents the decaying stage of the cloud induced by the evaporation process that decreases both CDR and COT. This triangular characteristic composed of the arrows A, B, and C simply models the life cycle of a single warm cloud in terms of microphysical particle growth processes; it may be employed to interpret the basic aspects of observed CDR–COT relationships as shown in Figs. 1 and 2.

The tendencies of CDR and COT associated with condensation and collection processes can further be understood in terms of the change in size distribution function due to these processes. As shown in Fig. 3, the size distribution function evolves through the condensation growth in the early stage and through the collection process in the mature stage. To investigate how these changes in size distribution function relate to the changes in CDR and COT, we consider the cross section σ , total mass concentration L , and effective radius r_e that are defined with the size distribution function $f(r)$ as

$$\sigma \propto \int_0^{+\infty} f(r)r^2 dr, \quad L \propto \int_0^{+\infty} f(r)r^3 dr, \quad r_e \propto \frac{L}{\sigma}.$$

The normalized rate of change in σ is then given from those in L and r_e as

$$\frac{1}{\sigma} \frac{d\sigma}{dt} = \frac{1}{L} \frac{dL}{dt} - \frac{1}{r_e} \frac{dr_e}{dt}. \quad (6)$$

Equation (6) means that σ increases (decreases) with time when the rate of change in mass concentration (dL/dt)/ L is larger (smaller) than that in effective radius (dr_e/dt)/ r_e . This leads to a positive (negative) correlation between σ and r_e .

Figure 8 shows how each term of (6) changes as a function of r_e through the evolution of size distribution

function for specified values of supersaturation. It is shown in the figures that the change rate of effective radius tends to decrease with increasing r_e up to around $r_e \sim 13\text{--}16 \mu\text{m}$ because of the nature of condensation process that decelerates the particle growth, followed by an increase in the change rate with increasing r_e due to the collection process that accelerates the particle growth. The change rate of mass concentration is found to monotonically decrease with increasing r_e , from positive values due to condensational growth toward zero due to the mass conservation induced by the collection process.

These tendencies of the change rates of r_e and L determine the change rate of σ according to (6). The change rate of σ decreases with increasing r_e from positive to negative values. The positive values take place for smaller r_e values where the change rate of L is larger than that of r_e because of the dominance of condensation process. The negative values are the result of the dominance of collection process that yields change rates of r_e larger than those of L .

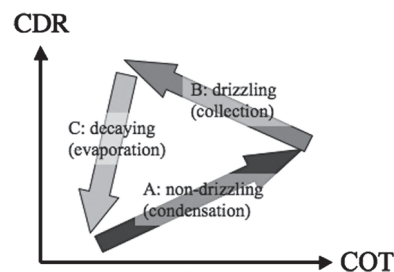


FIG. 7. Schematic diagram representing the tendencies of CDR and COT at the nondrizzling (A), drizzling (B), and decaying (C) stages of a single warm cloud development, induced by condensation, collection, and evaporation processes, respectively (see text for details).

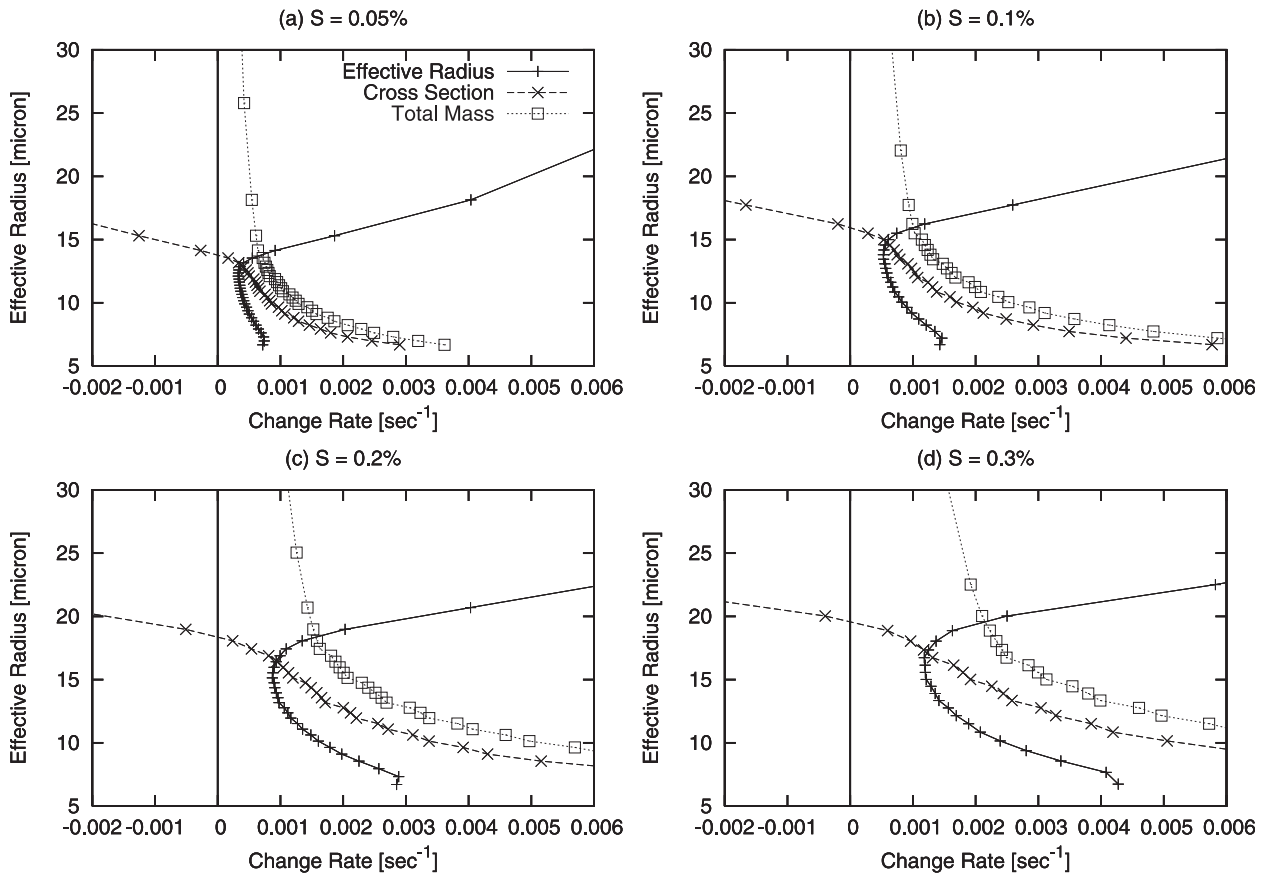


FIG. 8. The normalized change rate of effective radius, mass concentration, and cross section taken for abscissa as a function of effective radius (ordinate) through the evolution of size distribution function for given supersaturation values of $S =$ (a) 0.05%, (b) 0.1%, (c) 0.2%, and (d) 0.3%.

Figure 8 also shows that the plot of change rates for higher values of supersaturation tend to be stretched in both horizontal and vertical axis directions, corresponding to more amplified changes in the change rates through evolution of size spectra as a function of effective radius. These results for different values of supersaturation suggest how the change rates of r_e , σ , and L may be influenced by environmental conditions of aerosol concentration and dynamical stability, since the supersaturation is determined by these conditions through the competing effect between the forcing due to upward air motion and the damping due to condensation. The former is determined from dynamical stability condition and the latter depends on abundance of cloud particles resulting from aerosol number concentration. The higher (lower) values of supersaturation typically tend to occur under the condition of lower (higher) aerosol number concentrations and lower (higher) dynamical stabilities. The results shown in Fig. 8 suggest that the aerosol and dynamical conditions tend to modify the amplitude of change in the change rates of r_e , σ , and L although the

evolution patterns of these change rates, such as the positive-to-negative switching in σ , are qualitatively unchanged regardless of the environmental conditions.

Figure 9 schematically summarizes how the size distribution function expressed in mass concentration tends to evolve through these processes and how the changes in r_e and L take place. When the condensation controls the particle growth, the size distribution function tends to expand in vertical dimension, corresponding to the increase in mass concentration L , rather than shifting in horizontal dimension as represented by the effective radius r_e (Fig. 9, left panel). This tendency keeps the size spectrum narrow and produces the increasing tendency of σ , leading to the positive correlation between σ and r_e . When the collection process becomes active, on the contrary, the size distribution function tends to stop growing in vertical dimension and to shift in horizontal dimension, corresponding to the increase in effective radius r_e (Fig. 9, right panel). This leads to a spectral broadening and the tendency of σ then becomes negative (decreasing) in this case, providing the negative

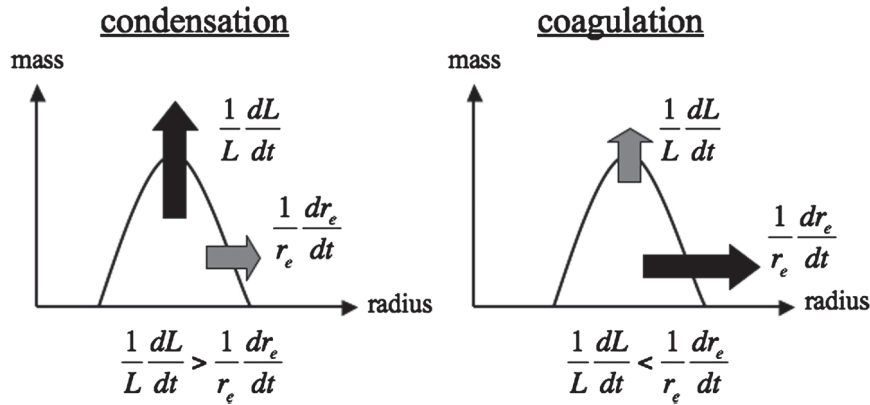


FIG. 9. Schematic illustration of evolution pattern of size distribution function due to (left) condensation and (right) collection particle growth processes, showing the tendencies of the growth rate of mass concentration and effective radius that determine the sign of correlation between the effective radius and the cross section (see text for details).

correlation between σ and r_e . The positive and negative correlation patterns between σ and r_e , thus derived from the evolution pattern of size spectra, are a fundamental cause of the correlation patterns between CDR and COT shown in Figs. 5 and 6. These results suggest that the satellite-observed positive and negative correlation patterns as shown in Figs. 1 and 2 may be correctly interpreted as being formed by condensation and collection processes through the change in size distribution function.

5. Dynamical and aerosol effects

The microphysical processes, which were found to form the positive and negative correlation patterns in the previous section, take place in a manner that depends on dynamical stability condition and aerosol amount. To examine how these environmental factors influence the CDR–COT correlation statistics, sensitivity experiments of changing these conditions are performed and the results are shown in this section.

a. Adiabatic model

Before showing the results from the sensitivity experiments, we review a conceptual cloud model based on a theoretical consideration of adiabatic growth of cloud particles suggested by previous studies (e.g., Brenguier et al. 2000) as a basis for interpreting the simulated results. In this model, the cloud water content q (in g m^{-3}) is assumed to linearly increase with height h as

$$q = \lambda h, \quad (7)$$

where λ is a constant parameter determined from pressure and temperature and is assumed to be $2.0 \times 10^{-3} \text{ g m}^{-4}$

in this study. The volume-averaged particle radius r_v is then given by

$$r_v(h) = \left(\frac{3}{4\pi\rho_w} \frac{q}{N_c} \right)^{1/3} = A^{1/3} h^{1/3} N_c^{-1/3},$$

where ρ_w and N_c denote the liquid water density and the cloud particle number concentration, respectively, and $A = 3\lambda/(4\pi\rho_w)$. The effective radius r_e is related with r_v as $r_e = k^{-1/3} r_v$ through the parameter k that varies from about 0.67 in continental air masses to about 0.80 in maritime air masses (Pontikis and Hicks 1992; Martin et al. 1994). The value of $k^{-1/3}$ then varies from about 1.08 to 1.14 and is assumed to be 1.1 in this study. The effective radius r_e is thus given from r_v as

$$r_e(h) = A^{1/3} h^{1/3} (kN_c)^{-1/3}. \quad (8)$$

This gives the effective radius at cloud top $h = H$ as

$$r_e(H) = A^{1/3} H^{1/3} (kN_c)^{-1/3}. \quad (9)$$

In the adiabatic growth model, cloud particles are considered to grow through condensation process where the number concentration N_c is assumed to be constant. Vertical integration of (7) and (8) over cloud layer of thickness H then leads to the expression for liquid water path W and optical thickness τ_c as

$$W = \int_0^H q \, dh = \frac{1}{2} \lambda H^2 \quad \text{and} \quad (10)$$

$$\tau_c = \frac{Q_{\text{ext}} \pi}{\rho_w 4/3\pi} \int_0^H \frac{q}{r_e} \, dh = \frac{3}{5} Q_{\text{ext}} \pi A^{2/3} (kN_c)^{1/3} H^{5/3}. \quad (11)$$

Equations (9) and (11) demonstrate that $r_e(H)$ and τ_c are related through the parameters N_c and H as discussed by previous studies (e.g., Brenguier et al. 2000; Szczodrak et al. 2001). The parameter H can be replaced with W since these two quantities are uniquely related through (10); thus, (9) and (11) can be rewritten in terms of N_c and W as

$$r_e(H) = A^{1/3} \left(\frac{2W}{\lambda} \right)^{1/6} (kN_c)^{-1/3} \propto W^{1/6} N_c^{-1/3} \quad \text{and}$$

$$\tau_c = \frac{3}{5} Q_{\text{ext}} \pi A^{2/3} (kN_c)^{1/3} \left(\frac{2W}{\lambda} \right)^{5/6} \propto W^{5/6} N_c^{1/3}.$$

These formulas provide theoretical relationships between $r_e(H)$ and τ_c under constant values of N_c and W as

$$\tau_c = \frac{8}{5} (\pi k)^2 \frac{\rho_w}{\lambda} N_c^2 r_e(H)^5 \propto N_c^2 r_e(H)^5 \quad \text{and} \quad (12)$$

$$\tau_c = \frac{9}{5} \frac{1}{\rho_w} \frac{W}{r_e(H)} \propto \frac{W}{r_e(H)}. \quad (13)$$

The relationship (12) for specified values of N_c is shown as solid curves in Figs. 10 and 11 and represents theoretical growth curves through the condensation process for those values of N_c . The value of W , which determines the relationship (13) shown as dotted curves in Figs. 10 and 11, represents the vertical extent that the cloud layer reaches. The theoretical curve (13) corresponding to larger value of W is then expected to trace the plot for more dynamically unstable conditions.

b. Dynamical effects

Figure 10 shows the CDR–COT scatterplots obtained from the sensitivity experiment of changing Γ_1 as $\Gamma_1 = 7.5$ (Fig. 10a), 8.0 (Fig. 10b), and 8.5 K km⁻¹ (Fig. 10c). These results are obtained from the simulation with aerosol amount f_{sfc} ranging from 7.8×10^5 to 1.8×10^6 m⁻³ approximately corresponding to $N_a \sim 10^{12}$ m⁻². These plots are overlaid on the theoretical relationships between CDR and COT for specified values of N_c and W given by (12) and (13).

Figure 10 indicates that the scatterplot is confined to the area of COT < 40 under the stable condition (Fig. 10a), whereas the maximum COT reaches about 120 under the unstable condition (Fig. 10c) without significant change in CDR values. It is also found that the CDR–COT correlation patterns are not significantly changed by the change in dynamical condition. The implied values of W observed by these plots are about $W < 300$ g m⁻² for the stable case (Fig. 10a) and tend to increase for more unstable cases, reaching the values larger than 1000 g m⁻²

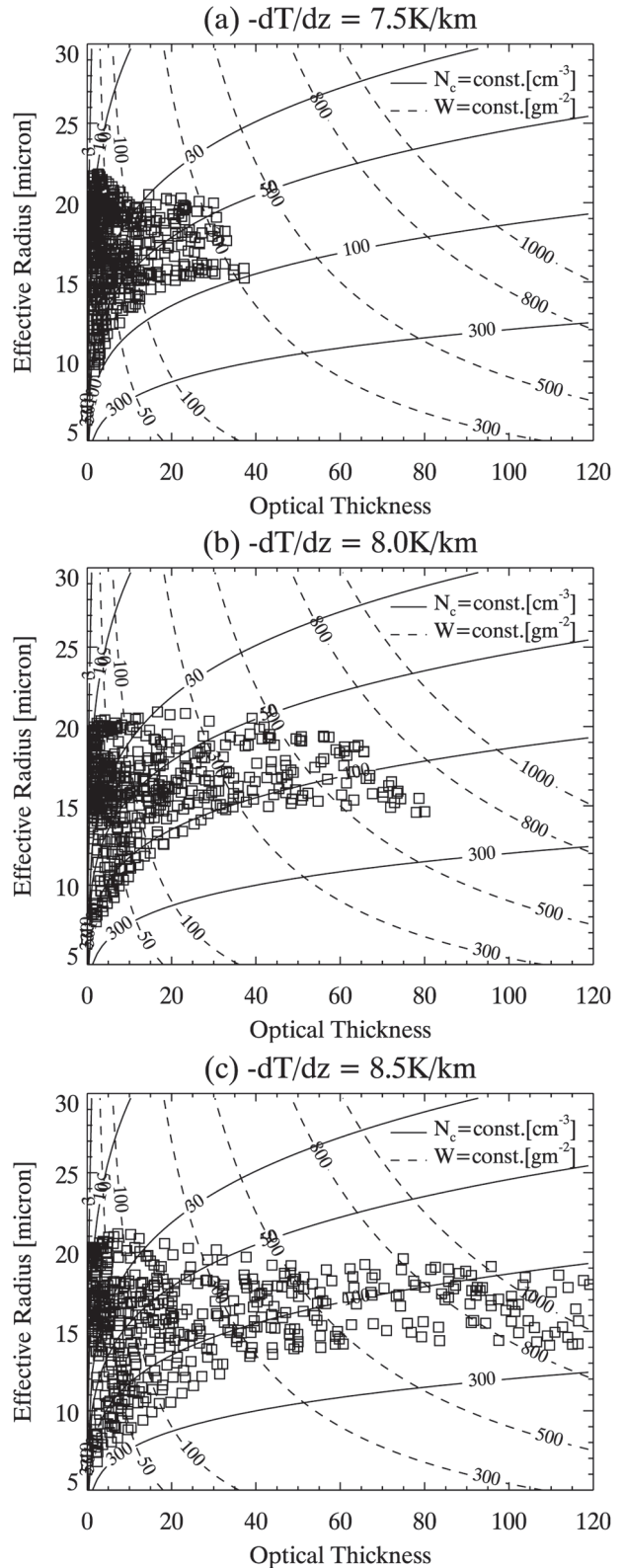


FIG. 10. Scatterplot between effective radius and optical thickness obtained from the simulation for $\Gamma =$ (a) 7.5, (b) 8.0, and (c) 8.5 K km⁻¹. The theoretical relationships (12) and (13) for specified values of N_c and W are also shown for reference as solid and dashed curves, respectively.

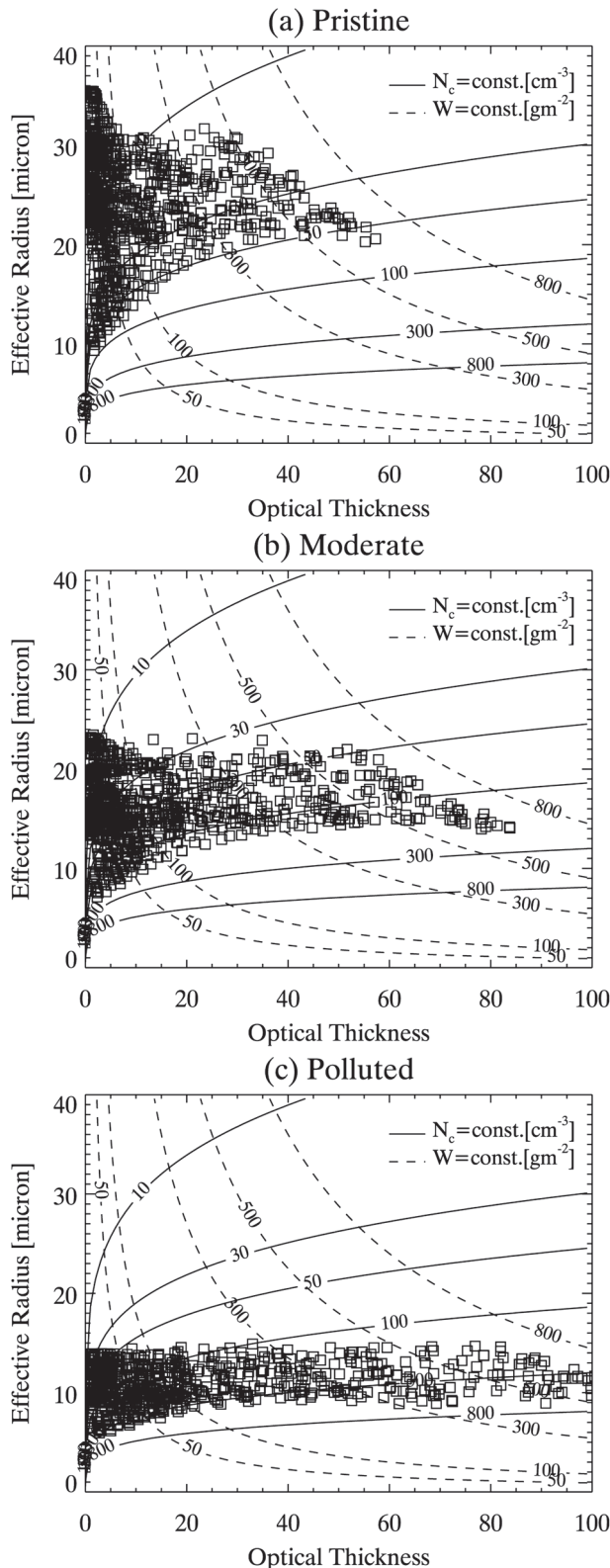


FIG. 11. Scatterplot between effective radius and optical thickness obtained from the simulation for (a) pristine, (b) moderate, and (c) polluted air conditions. The theoretical relationships (12) and (13) for specified values of N_c and W are also shown for reference as solid and dashed curves, respectively.

for the most unstable case (Fig. 10c). These results suggest that the change in dynamical stability condition tends to change the amplitude of the correlation plot through the change in liquid water path W without significantly changing the correlation patterns between CDR and COT.

c. Aerosol effects

Figure 11 shows the results from the sensitivity experiment of changing the aerosol amount by changing the parameter f_{sfc} from 10^5 to 10^6 m^{-3} for the “pristine” case (Fig. 11a), from 10^6 to 10^7 m^{-3} for the “moderate” case (Fig. 11b) and from 10^7 to 10^8 m^{-3} for the “polluted” case (Fig. 11c). These ranges of f_{sfc} values roughly correspond to surface aerosol number concentrations n_a of about 10^7 – 10^8 , 10^8 – 10^9 , and 10^9 – 10^{10} m^{-3} , respectively, and to column aerosol particle numbers N_a of about 10^{10} – 10^{11} , 10^{11} – 10^{12} , and 10^{12} – 10^{13} m^{-2} , respectively. The dynamical stability condition was assumed to be $\Gamma_1 = 8.0 \text{ K km}^{-1}$ for these experiments. These figures also include the theoretical relationships between CDR and COT for specified values of N_c and W given from the adiabatic growth model [(12) and (13)].

Figure 11 indicates that the CDR–COT relationship is significantly modified with the change in aerosol amount. The least squares fitting of the relationship $r_e \propto \tau_c^b$ to the scatterplots resulted in values of b of -0.024 , 0.0013 , and 0.03 for the clean, moderate, and polluted cases, respectively, demonstrating a change in correlation pattern between CDR and COT. It is also found that the scatterplot for the pristine condition (Fig. 11a) is located around larger values of CDR and relatively smaller values of COT compared to those for the moderate and polluted conditions (Figs. 11b and 11c) that are located around smaller values of CDR and reach larger values of COT. The more polluted case (Fig. 11c) tends to have smaller CDR values than the moderate case (Fig. 11b). This systematic change in scatterplot is found to correspond to the change in number concentration N_c implied from the adiabatic model: more polluted cases correspond to larger values of N_c . This change in CDR–COT plot is also found to occur in accordance with a constant value of W implied from the adiabatic model, which tends not to be affected by aerosol amount. These results suggest that the modification of the CDR–COT correlation plot with aerosols takes place through the change in particle number concentration N_c without significantly changing the liquid water path W .

It is worth noting that the plot shown in Fig. 11c is confined to CDR less than about $15 \mu\text{m}$ and the lower edge of the plot roughly follows the condensational growth curve (12) corresponding to $N_c = 300 \text{ cm}^{-3}$. This feature can be understood in terms of the nonlinear

behavior of Long's collection kernel function, which includes a threshold value of particle size that distinctively divides the inactive and active states of collection process. When aerosol amount is high, more numerous cloud droplets are produced from abundant aerosols. The higher number of cloud droplets tends to consume the water vapor more efficiently through the condensation process, leading to lower values of supersaturation, which in turn slow down the condensation process according to (2). This reduction in condensational growth speed tends to confine the CDR values to those smaller than critical radius of Long's kernel function and to prevent the collection process from becoming active.

The shape of the lower edge of the plot shown in Fig. 11c can also be interpreted with the findings of Szczodrak et al. (2001), who reported that a power-law relationship of the form $r_e \propto r_c^b$, with $b = 0.2$, well explains many cases of their observed analysis over the northeastern Pacific. Since this relationship is equivalent with (12) for a constant N_c value, their results may imply that the condensation process controls the CDR–COT statistics obtained from their analysis. There has been found, however, a much wider range of values for b by Eitzen et al. (2008) using a tropical cloud observation obtained from Visible/Infrared Scanner (VIRS) onboard the Tropical Rainfall Measuring Mission (TRMM) satellite. They performed a cluster analysis for CDR and COT observed data and found several clusters with distinctive positive and negative values of b as well as a cluster with b close to zero. Although the clusters of positive and negative b values may imply the existence of microphysical regimes controlled by condensation and collection processes, respectively, the observed variety of b values suggests more complicated situations in real clouds, especially on the global scale. These global-scale observations may be explained as a complex mixtures of simple condensation and collection tendencies shown in Fig. 7 that systematically change with environmental factors, as demonstrated in this section.

6. Discussion

The model results shown above demonstrate how the CDR–COT correlation patterns are formed through microphysical particle growth processes and how they tend to be influenced by environmental factors of aerosol and dynamical conditions. These findings of this study provide a basis for interpreting the correlation plot observed by previous remote sensing studies as shown in Figs. 1 and 2. In this section, we discuss several aspects of the observed CDR–COT correlation plot that may be explained by the model results in terms of the microphysical processes under various environmental conditions.

The positive and negative correlations mainly found for ASTEX (Fig. 2) and FIRE (Fig. 1), respectively, suggest that the clouds over the ASTEX region observed on this occasion are mainly at the condensation regime whereas many of the clouds observed over the FIRE region are interpreted as being in the collection growth stage, according to the findings of this study. It should be noted that the observed plots shown in Figs. 1 and 2 are for specific dates and times over these regions and the microphysical regimes suggested here are also for these specific observed cases. Similar interpretations, however, can be applied to other cases given the CDR–COT correlation plots obtained from observations.

Many panels of the correlation plot shown in Fig. 1 are also found to have a small portion of positive correlation under the large part of negative correlation as typically shown in panels B3, C1, C3, C4, D2, and D3 of Fig. 1. These small parts of positive correlation appear to trace the theoretical curve (12) that corresponds to relatively small values of number concentration N_c , similar to our model results for pristine condition shown in Fig. 11a. This is possibly induced by the pristine air mass conditions over the FIRE region. The smaller values of number concentrations associated with pristine aerosol conditions may cause a large amount of drizzle particles, found as a large portion of negative correlation in many panels of Fig. 1. Our previous modeling study (Suzuki et al. 2006) also simulated a correlation pattern closely similar to those observed over the FIRE region when the pristine aerosol condition was assumed in the model. The left edge of the large negative correlation part may include the evaporation stage characterized by decreasing tendencies of both CDR and COT, which are simulated by the model as shown in Fig. 6.

The ASTEX region, on the contrary, tends to include only the positive correlation branch in many cases, as typically shown in panels A1, A2, B1, B2, C1, C2, and D1 of Fig. 2. These plots tend to cover smaller CDR values than the FIRE case and to coincide with the theoretical curve (12) corresponding to larger values of N_c , possibly because of a polluted aerosol condition over the ASTEX region. This result also confirms our previous study (Suzuki et al. 2006) that simulated the correlation plot similar to those found over the ASTEX region when turbid air conditions are assumed in the model. The polluted aerosol conditions may suppress the drizzle formation, which is shown as an absence of negative correlation part in many panels of Fig. 2. These observed characteristics with only a positive correlation branch are similar to our model result over polluted conditions (Fig. 11c), which also tends to include only a positive correlation branch.

Besides these remarkable characteristics, several interesting features are also found in these observed

scatterplots. Panels D1 and D4 of Fig. 1 are found to have two branches that are likely to trace the theoretical curve [(12)] corresponding to two distinct values of number concentration N_c , implying that there exist two types of air masses with different aerosol amounts. Similar multibranch features can also be found in panels A4, B2, and B4 of Fig. 2, which also may imply the mixture of air masses characterized by different aerosol amounts. There can also be found scatterplots with different amplitudes characterized by different magnitudes of COT values. The panels A1, B1, and C1 of Fig. 1 and A1, A4, B4, and C4 of Fig. 2 tend to have smaller magnitudes compared to other plots. These differences in magnitudes can be interpreted as being induced by different dynamical conditions as shown in our model simulation (Fig. 10). Various characteristics found in observed correlation plots so far reported can thus be explained by different aerosol and dynamical conditions through their effects on microphysical particle growth processes.

7. Conclusions

This study investigated the microphysical mechanisms that control the CDR–COT relationships using a non-hydrostatic spectral bin microphysics cloud model. The numerical experiments were performed to form low-level warm clouds under various aerosol and dynamical stability conditions. The results showed positive and negative correlation patterns between CDR and COT for nondrizzling and drizzling stages of cloud development, similar to those reported by previous remote sensing studies. It was found that only the positive correlation pattern was simulated when the collection process was switched off in the model, whereas both the positive and negative correlation branches were reproduced when the model included the collection as well as condensation processes. The positive and negative correlations were also found to be explained by evolution patterns of the size distribution function due to the condensation and collection processes, respectively.

Sensitivity experiments of changing the aerosol and dynamical conditions were also performed. It was shown that the change in dynamical condition tends to change the amplitude of the CDR–COT scatterplot, especially in COT direction, without changing their correlation patterns, whereas the change in aerosol amount has an effect of modifying the correlation pattern between CDR and COT through changing CDR values. The former and latter changes are found to correspond to the change in liquid water path and number concentration, respectively, as implied from an adiabatic growth model. These findings provide a basis for interpreting the various characteristics found in observed CDR–COT correlation

plots obtained by previous observational studies, and they may also help improve the parameterizations employed in climate models for more realistic simulations of cloud microphysical properties and their interactions with aerosols.

Acknowledgments. The authors are grateful to Matt Lebsock and two anonymous reviewers for their valuable comments on earlier version of the manuscript. This study was supported by JAXA/EarthCARE, MEXT/VL for Climate System Diagnostics, MOE/Global Environment Research Fund B-083, JST/CREST, and MEXT/Innovative Program of Climate Change Projection for the 21st Century.

REFERENCES

- Asano, S., M. Shiobara, and A. Uchiyama, 1995: Estimation of cloud physical parameters from airborne solar spectral reflectance measurements for stratocumulus clouds. *J. Atmos. Sci.*, **52**, 3556–3576.
- Boers, R., and L. D. Rotstain, 2001: Possible links between cloud optical depth and effective radius in remote sensing observations. *Quart. J. Roy. Meteor. Soc.*, **127**, 2367–2383.
- Bott, A., 1989: A positive definite advection scheme obtained by nonlinear renormalization of the advective fluxes. *Mon. Wea. Rev.*, **117**, 1006–1016.
- , 1998: A flux method for the numerical solution of the stochastic collection equation. *J. Atmos. Sci.*, **55**, 2284–2293.
- Brenguier, J.-L., H. Pawlowska, L. Schüller, R. Preusker, J. Fischer, and Y. Fouquart, 2000: Radiative properties of boundary layer clouds: Droplet effective radius versus number concentration. *J. Atmos. Sci.*, **57**, 803–821.
- Bretherton, C. S., S. K. Krueger, M. C. Wyant, P. Bechtold, E. van Meijgaard, B. Stevens, and J. Teixeira, 1999: A GCSS boundary-layer cloud model intercomparison study of the first ASTEX Lagrangian experiment. *Bound.-Layer Meteor.*, **93**, 341–380.
- Eitzen, Z. A., K.-M. Xu, and T. Wong, 2008: Statistical analyses of satellite cloud object data from CERES. Part V: Relationships between physical properties of marine boundary layer clouds. *J. Climate*, **21**, 6668–6688.
- Feingold, G., and S. M. Kreidenweis, 2002: Cloud processing of aerosol as modeled by a large eddy simulation with coupled microphysics and aqueous chemistry. *J. Geophys. Res.*, **107**, 4687, doi:10.1029/2002JD002054.
- , W. R. Cotton, S. M. Kreidenweis, and J. T. Davis, 1999: The impact of giant cloud condensation nuclei on drizzle formation in stratocumulus: Implications for cloud radiative properties. *J. Atmos. Sci.*, **56**, 4100–4117.
- Han, Q., W. B. Rossow, and A. A. Lacis, 1994: Near-global survey of effective droplet radii in liquid water clouds using ISCCP data. *J. Climate*, **7**, 465–497.
- , —, J. Chou, and R. M. Welch, 1998: Global survey of the relationships of cloud albedo and liquid water path with droplet size using ISCCP. *J. Climate*, **11**, 1516–1528.
- Iguchi, T., T. Nakajima, A. P. Khain, K. Saito, T. Takemura, and K. Suzuki, 2008: Modeling the influence of aerosols on cloud microphysical properties in the East Asia region using a meso-scale model coupled with a bin-based cloud microphysics scheme. *J. Geophys. Res.*, **113**, D14125, doi:10.1029/2007JD009774.

- Kawamoto, K., T. Nakajima, and T. Y. Nakajima, 2001: A global determination of cloud microphysics with AVHRR remote sensing. *J. Climate*, **14**, 2054–2068.
- Khain, A., and I. Sednev, 1996: Simulation of precipitation formation in the eastern Mediterranean coastal zone using a spectral microphysics cloud ensemble model. *Atmos. Res.*, **43**, 77–110.
- , and A. Pokrovsky, 2004: Simulation of effects of atmospheric aerosols on deep turbulent convective clouds using a spectral microphysics mixed-phase cumulus cloud model. Part II: Sensitivity study. *J. Atmos. Sci.*, **61**, 2983–3001.
- , —, and I. Sednev, 1999: Some effects of cloud–aerosol interaction on cloud microphysics structure and precipitation formation: Numerical experiments with a spectral microphysics cloud ensemble model. *Atmos. Res.*, **52**, 195–220.
- , —, A. Pinsky, A. Seifert, and V. Phillips, 2004: Simulation of effects of atmospheric aerosols on deep turbulent convective clouds using a spectral microphysics mixed-phase cumulus cloud model. Part I: Model description and possible applications. *J. Atmos. Sci.*, **61**, 2963–2982.
- Kobayashi, T., and K. Masuda, 2008: Effects of precipitation on the relationships between cloud optical thickness and drop size derived from space-borne measurements. *Geophys. Res. Lett.*, **35**, L24809, doi:10.1029/2008GL036140.
- Lebsock, M. D., G. L. Stephens, and C. Kummerow, 2008: Multi-sensor satellite observations of aerosol effects on warm clouds. *J. Geophys. Res.*, **113**, D15205, doi:10.1029/2008JD009876.
- Lohmann, U., G. Tselioudis, and C. Tyler, 2000: Why is the cloud albedo–particle size relationship different in optically thick and optically thin clouds? *Geophys. Res. Lett.*, **27**, 1099–1102.
- Long, A. B., 1974: Solutions to the droplet collection equation for polynomial kernels. *J. Atmos. Sci.*, **31**, 1040–1052.
- Martin, G. M., D. W. Johnson, and A. Spice, 1994: The measurement and parameterization of effective radius of droplets in warm stratocumulus clouds. *J. Atmos. Sci.*, **51**, 1823–1842.
- Masunaga, H., T. Y. Nakajima, T. Nakajima, M. Kachi, and K. Suzuki, 2002: Physical properties of marine low clouds as retrieved by combined use of Tropical Rainfall Measuring Mission (TRMM) microwave imager and visible/infrared scanner. 2. Climatology of warm clouds and rain. *J. Geophys. Res.*, **107**, 4367, doi:10.1029/2001JD001269.
- Matsui, T., H. Masunaga, R. A. Pielke Sr., and W.-K. Tao, 2004: Impact of aerosols and atmospheric thermodynamics on cloud properties within the climate system. *Geophys. Res. Lett.*, **31**, L06109, doi:10.1029/2003GL019287.
- Nakajima, T., and M. D. King, 1990: Determination of the optical thickness and effective particle radius of clouds from reflected solar radiation measurements. Part I: Theory. *J. Atmos. Sci.*, **47**, 1878–1893.
- , —, J. D. Spinhirne, and L. F. Radke, 1991: Determination of the optical thickness and effective particle radius of clouds from reflected solar radiation measurements. Part II: Marine stratocumulus observations. *J. Atmos. Sci.*, **48**, 728–751.
- Nakajima, T. Y., and T. Nakajima, 1995: Wide-area determination of cloud microphysical properties from NOAA AVHRR measurements for FIRE and ASTEX regions. *J. Atmos. Sci.*, **52**, 4043–4059.
- Peng, Y., U. Lohmann, R. Leitch, C. Banic, and M. Couture, 2002: The cloud albedo–cloud droplet effective radius relationship for clean and polluted clouds from RACE and FIRE. *J. Geophys. Res.*, **107**, 4106, doi:10.1029/2000JD000281.
- Pontikis, C. A., and E. Hicks, 1992: Contribution to the cloud droplet effective radius parameterization. *Geophys. Res. Lett.*, **19**, 2227–2230.
- Rogers, R. R., and M. K. Yau, 1989: *A Short Course in Cloud Physics*. Elsevier, 293 pp.
- Sato, Y., T. Nakajima, K. Suzuki, and T. Iguchi, 2009: Application of a Monte Carlo integration method to collision and coagulation growth processes of hydrometeors in a bin-type model. *J. Geophys. Res.*, **114**, D09215, doi:10.1029/2008JD011247.
- Slingo, A., 1989: A GCM parameterization for the shortwave radiative properties of water clouds. *J. Atmos. Sci.*, **46**, 1419–1427.
- Stone, J. M., and M. L. Norman, 1992: A radiation hydrodynamics code for astrophysical flows in two space dimensions. 1. The hydrodynamic algorithms and tests. *Astrophys. J.*, **80**, 753–790.
- Suzuki, K., 2004: A study on numerical modeling of cloud microphysics for calculating the particle growth process. Ph.D dissertation, University of Tokyo, 136 pp.
- , T. Nakajima, T. Y. Nakajima, and A. Khain, 2006: Correlation pattern between effective radius and optical thickness of water clouds simulated by a spectral bin microphysics cloud model. *SOLA*, **2**, 116–119.
- Szczodrak, M., P. H. Austin, and P. B. Krummel, 2001: Variability of optical depth and effective radius in marine stratocumulus clouds. *J. Atmos. Sci.*, **58**, 2912–2926.
- Takahashi, T., and T. Kawano, 1998: Numerical sensitivity study of rainband precipitation and evolution. *J. Atmos. Sci.*, **55**, 57–87.
- , and K. Shimura, 2004: Tropical rain characteristics and microphysics in a three-dimensional cloud model. *J. Atmos. Sci.*, **61**, 2817–2845.
- Van Leer, B., 1977: Towards the ultimate conservative difference scheme. IV. A new approach to numerical convection. *J. Comput. Phys.*, **23**, 276–299.